Journal of Materials Chemistry C

ROYAL SOCIETY OF CHEMISTRY

COMMUNICATION

View Article Online
View Journal

Check for updates

Cite this: DOI: 10.1039/d6tc00516k

Received 17th February 2026,
Accepted 20th April 2026

DOI: 10.1039/d6tc00516k

rsc.li/materials-c

On-demand optical printing of Ag-based neuromorphic devices for brain-inspired learning

Bharath Bannur * and Sajan D. George *

Open Access Article. Published on 21 April 2026. Downloaded on 5/12/2026 5:03:44 AM.
This article is licensed under a Creative Commons Attribution 3.0 Unported Licence.

Neuromorphic computing, in which memory and computation occur in the same physical system, promises to overcome the von Neumann bottleneck by mimicking the massively parallel architecture of biological neural networks. Self-formed networks with disordered, nonlinear connectivity are especially promising for synaptic plasticity, but fabrication often demands vacuum deposition or complex chemical processing, limiting broader accessibility and adoption. Here, we present the rapid, on-demand optical printing of an Ag nanoparticle assembly to form a continuous film, followed by an annealing method. The film spontaneously transforms into disconnected Ag nanostructures with tunable morphologies. By systematically varying the printing time and annealing conditions, we realize Ag-based neuromorphic devices showing reliable resistive switching, short- and long-term potentiation, and, importantly, arousal-dependent performance, classically described by the Yerkes–Dodson law, all achieved without external CMOS circuitry. This approach offers a reproducible, cost-effective, and scalable route to self-organized Ag networks, bypassing the constraints of traditional vacuum or chemically intensive methods. These devices, based on emergent architectures, open up pathways toward scalable, adaptive hardware for advanced neuromorphic computing.

Introduction

The pursuit of the replication of the human brain's computational prowess has spurred extensive research into the development of neuromorphic systems, aiming to emulate the brain's remarkable parallel in-memory processing and efficiency in executing complex tasks with minimal power consumption.[1,2] Traditional von Neumann architectures, which separate memory and logic, suffer from throughput limits and high energy costs due to frequent data transfer, posing a major obstacle for embedded or real-time applications in robotics, medical devices, and sensory systems.[3–5] To address this, neuromorphic computing, inspired by the biological brain, holds the promise of achieving unprecedented energy efficiency and real-time data processing capabilities by mimicking neural networks.[6–8] Physical implementations of artificial neural networks offer alternatives to conventional computing hardware, addressing concerns about energy consumption and processing speed. In this regard, memristive devices, which can emulate the behavior of biological synapses, have emerged as promising building blocks for neuromorphic systems.[9,10]

Neuromorphic devices have attracted significant interest in recent years as highly sought-after alternatives to conventional computing platforms.[11–14] They operate through various mechanisms such as ion migration,[15–17] phase change,[18–20] charge trapping–detrapping,[21–23] and electrochemical metallization.[24–27] Numerous organic and inorganic materials have been utilized as active elements in these devices to emulate synaptic functionalities such as paired-pulse facilitation (PPF),[28–30] spike-timing-dependent plasticity (STDP),[31,32] and metaplasticity,[33,34] to name a few. Among the many active elements explored, self-formed systems come much closer to mimicking the biological neural network both structurally and functionally. These systems, exhibiting disordered network structures with nonlinear interactions, give rise to emergent properties crucial for emulating synaptic functionalities.[35] Several self-formed systems have been reported in the literature, such as Ag nanowires[36–38] and Sn nanoparticles.[39–41] However, these often rely on exotic materials and complex fabrication routes. Recently, disconnected Ag artificial synaptic network (Ag ASN) structures obtained through dewetting were reported, resembling biological neural networks and exhibiting several higher-order learning abilities.[42,43] However, this approach required a sophisticated vacuum evaporation setup. A solution-processing method was later introduced to fabricate Ag ASNs, which successfully reproduced behavioral learning patterns.[44] Despite achieving the key properties needed for synaptic functionality, this strategy still relied on special precursors and demanded extensive optimization to yield the

Manipal Institute of Applied Physics, Manipal Academy of Higher Education, Manipal, 576104, India. E-mail: sajan.george@manipal.edu, bharath.b@manipal.edu

Open Access Article. Published on 21 April 2026. Downloaded on 5/12/2026 5:03:44 AM.
This article is licensed under a Creative Commons Attribution 3.0 Unported Licence.

desired architecture. In both cases, Ag ASN formation depended on thin-film fabrication through either vacuum deposition or complex solution coating. This highlights the need for a more effective approach that enables the spontaneous formation of such systems through simple, reliable processing.

Recently, printed neuromorphic devices have attracted considerable attention owing to their simplicity, scalability, and compatibility with wearable technologies, which are key enablers of the Industry 4.0 revolution.[45] While inkjet printing has been the dominant technique, optical printing offers a more straightforward and efficient route for on-demand fabrication, with the added advantage of achieving high-resolution features.[46–48] Nevertheless, only a limited number of studies have explored optically printed neuromorphic devices. For example, laser-induced graphene memristors[49] and laser-printed ZnO memristors[50] have been demonstrated, but these approaches typically rely on costly laser systems and complex ink formulations, and have thus far exhibited only basic memristive switching characteristics. Recently, we reported the first demonstration of the white-light-based optical printing of arbitrary plasmonic nanostructures, a simple yet powerful method to achieve mask-free, sub-micron resolution patterns.[51] In the present study, this simple and highly efficient optical printing approach, with modified optics, has been utilized to deposit a continuous particulate Ag film for developing artificial neuromorphic devices. The resulting films were annealed to obtain disconnected Ag islands, commonly referred to as Ag artificial synaptic networks (Ag-ASNs), for realizing neuromorphic devices. Various control parameters were analyzed to achieve the desired active geometry. An Ag neuromorphic device was fabricated, and its switching behavior was studied. Synaptic functionalities such as short-term plasticity (STP) and long-term potentiation (LTP) were emulated. Notably, arousal-dependent learning and memory, classically described by the Yerkes–Dodson law[52] and representing a fundamental human behavioral pattern, were also emulated in the device without any external CMOS circuitry. Importantly, this approach provides a cost-effective and accessible alternative to conventional fabrication methods by eliminating the need for sophisticated vacuum systems or complex chemical processing, while enabling the direct, on-demand patterning of Ag structures. In addition, the localized printing significantly reduces material wastage and is inherently compatible with scalable, parallel device fabrication. This study demonstrates an innovative approach for fabricating an Ag neuromorphic device and emulating higher-order synaptic functionalities.

Results and discussion

The goal of obtaining a continuous Ag film without the involvement of time-consuming, sophisticated vacuum deposition or complex solution techniques was achieved using optical printing. A schematic of the printing setup is shown in Fig. 1a. In brief, white light from a digital light processing (DLP)-based projector was coupled to a 10× objective lens of a microscope using an eyepiece, a −100 mm planoconcave lens, a 300 mm biconvex lens, and a dichroic mirror to collimate, adjust the magnification, and steer the beam. A 100 μL drop of Ag nanoparticles, synthesized using the standard citrate reduction method,[53] was placed on a glass slide positioned on the microscope stage, and a rectangular white-light pattern was illuminated onto the sample (Fig. S1, SI). The plasmonic absorption peak was found at ∼419 nm with an average particle size of ∼82 nm (Fig. S2, SI). White light containing the plasmonic resonance wavelength was absorbed by the nanoparticles, resulting in localized heating and the formation of thermal gradients in the illuminated region. These gradients generated density-driven (buoyancy) convection and surface-tension-driven (Marangoni) flows within the surrounding fluid, directing nanoparticles toward the substrate. When convective transport overcame the electrostatic repulsion between the nanoparticles and the substrate, the particles achieved close contact and adhered *via* van der Waals interactions.[48] This process enabled the precise immobilization and patterned deposition of nanoparticles onto the substrate without the need for chemical functionalization or elevated bulk temperatures.

Printing was performed for different durations between 1 and 9 minutes to obtain continuous films. Optical images in reflection (transmission) mode for 3, 6, and 9 minutes are shown in Fig. 1b–d (Fig. S3, Supplementary Information). The reflectance (opacity) of the prints increased with printing time, suggesting improved particle connectivity leading to particulate film formation. To gain detailed insights into the film morphology, FESEM imaging was performed on the printed regions (Fig. 1e–g). For 3 minutes of printing (Fig. 1e), the particles formed a networked arrangement with limited area coverage. With 6 minutes of printing (Fig. 1f), the connectivity improved, and with 9 minutes (Fig. 1g), the areal coverage increased further with additional overlayer growth. Fill factor (FF, percentage of areal coverage) analysis performed on the FESEM images using ImageJ (Fig. S4, SI) showed a gradual increase in FF (Fig. 1h), from ∼43% with 3 minutes of printing to ∼90% with 9 minutes, validating continuous particulate film formation. Conductance measurements were performed to confirm film continuity (Fig. 1i). A linear voltage sweep (0–50 mV) was applied to the films with different printing times. Films printed for 3–6 minutes showed negligible currents, indicating high resistance (>10 GΩ) due to discontinuity. With 7 minutes of printing, the current increased slightly, with a drastic improvement at 8–9 minutes, reducing the resistance to ∼20 kΩ. The microscopic and electrical studies together indicate that increasing the printing time leads to continuous particulate films.

After obtaining continuous films at a printing time of 9 minutes, the annealing conditions were systematically investigated to form Ag artificial synaptic networks (Ag-ASN). The films were subjected to two different temperatures, 200 °C and 300 °C, and the corresponding annealing durations were optimized. Initially, the films were annealed at 200 °C for various durations (2–10 minutes). *I–V* Characteristics before and after annealing were analyzed (Fig. 2a). The average initial resistance of a 9-minute-printed film was ∼20 kΩ (Fig. 2a). With 2 and

 This journal is © The Royal Society of Chemistry 2026

Open Access Article. Published on 21 April 2026. Downloaded on 5/12/2026 5:03:44 AM.
This article is licensed under a Creative Commons Attribution 3.0 Unported Licence.

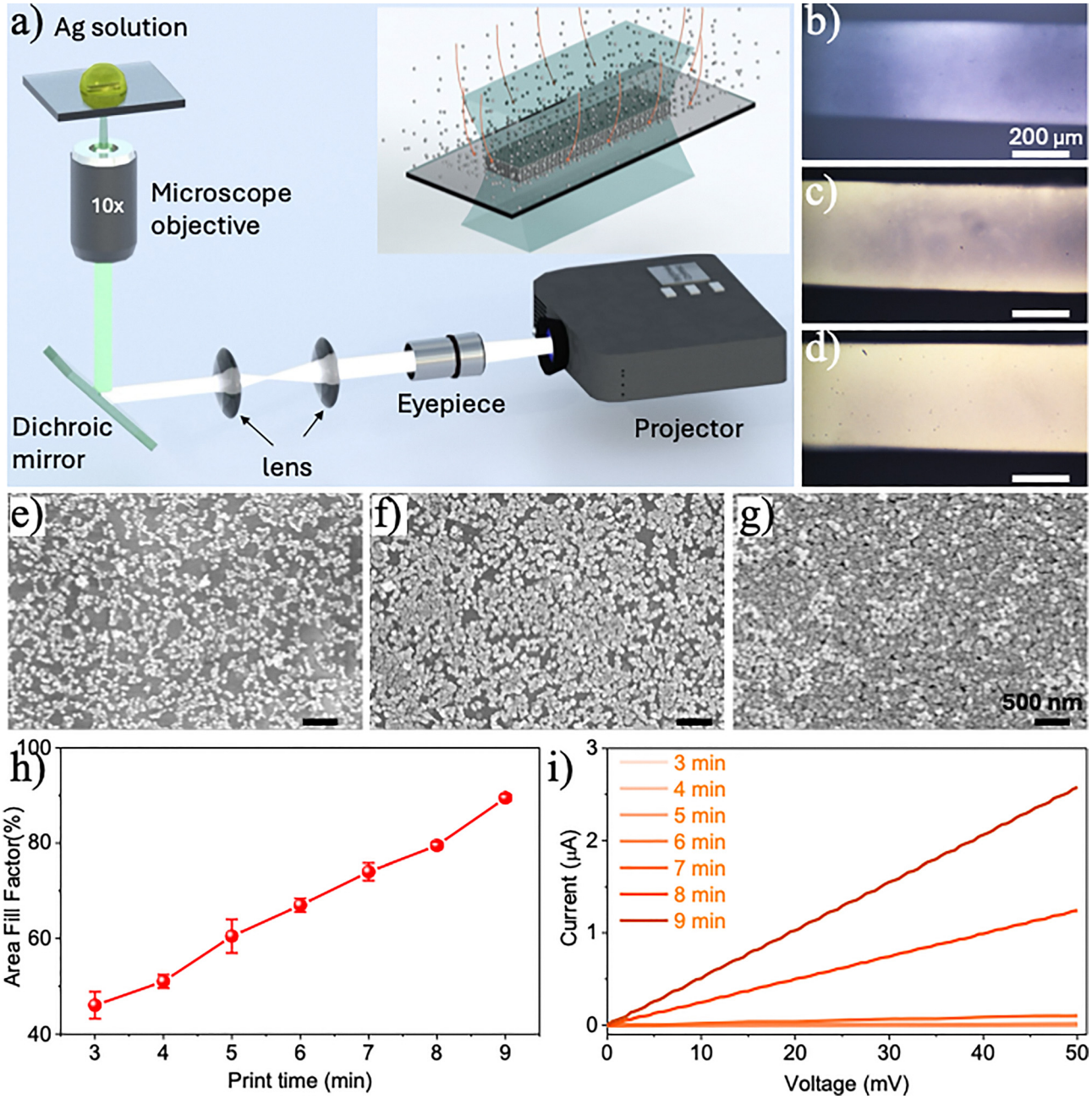

Fig. 1 Ag particulate film printing. (a) Schematic of the projection printing technique. (b)–(d) Optical microscope images (reflection mode) of the printed patterns after 3, 6, and 9 minutes of printing. (e)–(g) FESEM images of the corresponding patterns, showing improved nanoparticle deposition with time. (h) The fill factor increases with longer printing durations. (i) *I*–*V* Characteristics show a decrease in resistance with increasing printing time, confirming enhanced connectivity.

4 minutes of annealing, the resistance decreased by three orders of magnitude due to particle coalescence and enhanced connectivity. However, with annealing times of 6 minutes and longer, the resistance increased by four orders of magnitude, suggesting a non-conducting nature due to dewetting. Optical images (transmission mode) of the film before and after 10 minutes of annealing showed increased transparency, indicating a reduced fill factor and confirming dewetting (Fig. 2b and c). To confirm the emergence of disconnected Ag structures, FESEM images were captured (Fig. 2d–f and Fig. S5, SI). For 2–4 minutes of annealing, the particles fused into a better-connected network, explaining the conductance increase. In contrast, films annealed for durations above 6 minutes exhibited disconnected Ag structures consisting of larger particles (islands) along with smaller fragments (spherical particles). A closer analysis of samples annealed for 6 and 8 minutes reveals that increasing the annealing time leads to a systematic increase in inter-island gaps, accompanied by the fragmentation of larger islands into smaller, less branched structures. Specifically, the inter-island gaps for the 6-minute annealed sample are

Open Access Article. Published on 21 April 2026. Downloaded on 5/12/2026 5:03:44 AM.
This article is licensed under a Creative Commons Attribution 3.0 Unported Licence.

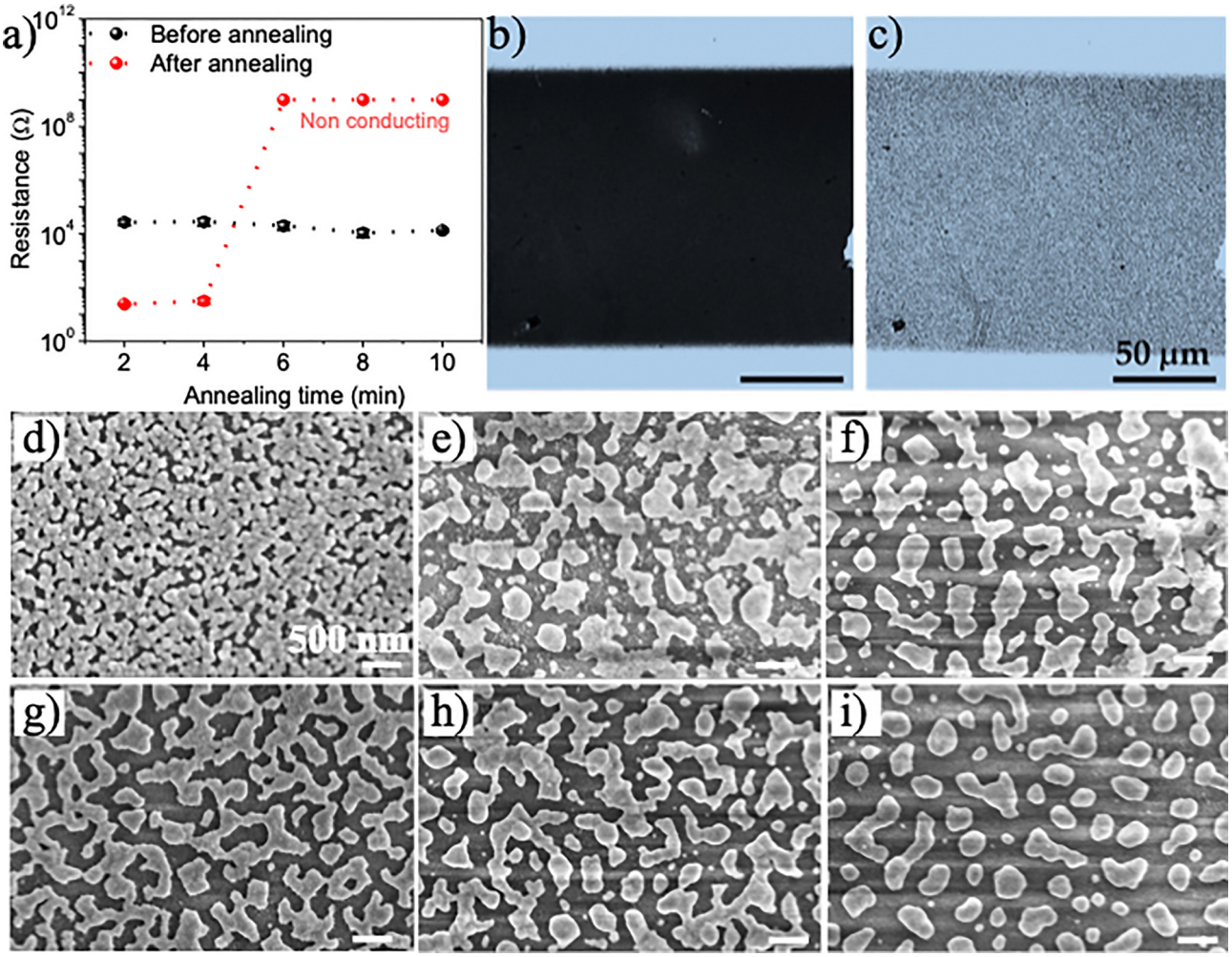

Fig. 2 Dewetting the Ag film. (a) Resistance variation of the printed patterns during annealing at different times. (b) and (c) Optical images (transmission mode) showing increased transmittance with annealing, indicative of island formation. (d)–(f) FESEM images of films annealed at 200 °C for 4, 6, and 8 minutes. (g)–(i) FESEM images of films annealed at 300 °C for 30, 60, and 120 s. (Scale bar: 500 nm.).

predominantly in the range of 30–100 nm, whereas for 8 minutes, the gaps shift to values above 100 nm, with the emergence of micron-scale separations (Fig. S6a and b). In addition, island fragmentation results in an increase in island density from $\sim 0.4 \times 10^9$ islands per square inch (6 minutes) to $\sim 0.8 \times 10^9$ islands per square inch (8 minutes). For the 10-minute annealing condition, although the average inter-island distance and island density ($\sim 0.8 \times 10^9$) remain comparable to the 8-minute case (Fig. S6c), the occurrence of larger gaps further increases. Films annealed at 300 °C for 30, 60, and 120 s also exhibited dewetting (Fig. 2g–i). After 30 s, the film remained largely continuous. At 60 s, well-defined disconnected islands with increased branching were observed, with an island density of $\sim 0.5 \times 10^9$ islands per square inch and inter-island gaps predominantly below 100 nm (Fig. S6d). Upon increasing the annealing time to 120 s, further fragmentation led to the formation of a higher proportion of spherical particles, resulting in a reduced island density ($\sim 0.4 \times 10^9$ islands per square inch) and larger inter-island gaps exceeding 200 nm, along with an increased occurrence of micron-scale separations (Fig. S6e). Thus, higher annealing temperatures significantly reduce the dewetting time, while prolonged annealing promotes fragmentation, spherical particle formation, and wider inter-island spacing. The dewetted structure resembles a biological neural network, with islands acting as neurons and branches as dendrites and axons (Fig. S7, SI). Interestingly, the measured island density range of $0.4–0.8 \times 10^9$ per square inch is close to the approximate 2D neuron density ($\sim 10^9$ per square inch) in the human brain.[42]

Neuromorphic devices were fabricated by exploiting the on-demand printing capability of the technique. Ag particulate films were printed across shadow-mask-based pre-fabricated Au electrodes (Fig. S8, Supplementary Information) and annealed at 200 °C to obtain dewetted structures. The *I–V* characteristics of a device annealed for 6 minutes are shown in Fig. 3a. Initially, the device showed low currents due to disconnected Ag structures, corresponding to the high-resistance state (HRS, non-conducting state). With increasing voltage up to ~14 V (forming voltage), an abrupt current increase was observed, reaching the set current compliance (I_{CC}) of 1 μA and transitioning to the low-resistance

 This journal is © The Royal Society of Chemistry 2026

Open Access Article. Published on 21 April 2026. Downloaded on 5/12/2026 5:03:44 AM.
This article is licensed under a Creative Commons Attribution 3.0 Unported Licence.

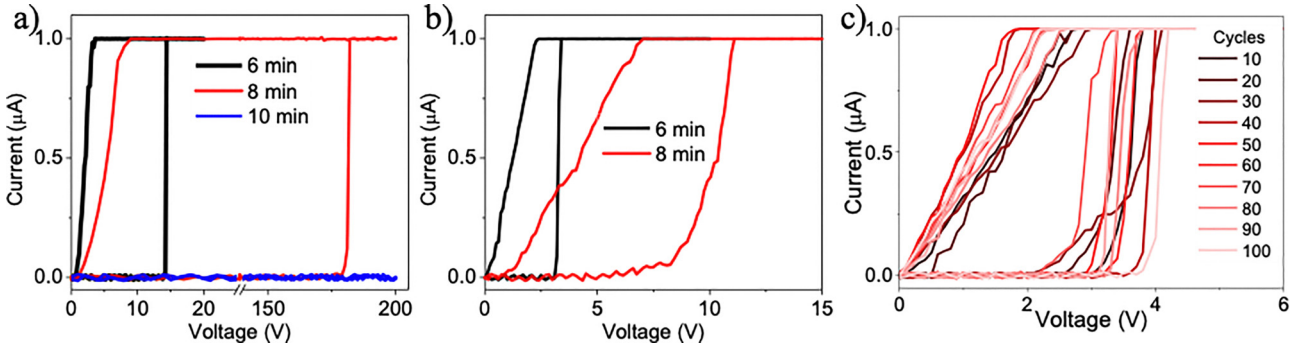

Fig. 3 Resistive switching characteristics. *I–V* Characteristics of the neuromorphic devices showing (a) forming voltages, (b) switching voltages, and (c) switching cycles demonstrating endurance.

state (LRS, conducting state). During the reverse sweep, the device remained in the LRS up to ~2 V before switching back to the HRS. This HRS-to-LRS transition arises from the electric-field-induced formation of Ag conduction paths, consistent with island-based devices. With 8 minutes of annealing, the forming voltage (V_{th}) was ~150 V, and with 10 minutes, switching did not occur even at 200 V. The current through the device was limited to 1 μA using a compliance setting to protect the device from damage during the high-voltage forming process. This indicates that increasing the annealing time decreases the island size and increases the inter-island gaps, hindering conduction path formation and requiring higher voltages for switching. After electroforming, however, devices required lower voltages to switch due to residual conduction paths facilitating low-voltage operation. The switching voltage (V_{th}) decreased to ~3 V for the 6-minute film compared to ~10 V for the 8 minute sample (Fig. 3b). Cyclic stability over 100 cycles was demonstrated with V_{th} maintained at 3.4 ± 0.4 V (Fig. 3c). A similar trend was observed for films dewetted at 300 °C: devices switched with V_{th} of ~3 ± 0.4 V for 60 s of annealing (Fig. S9, SI), while no switching was observed for 120 s dewetting. For subsequent studies, the device annealed at 200 °C for 6 minutes was selected.

Synaptic functionalities were then emulated in the device. Short-term plasticity (STP) and long-term potentiation (LTP) are crucial memory patterns in the human brain and serve as effective storage models for cognitive processes. According to

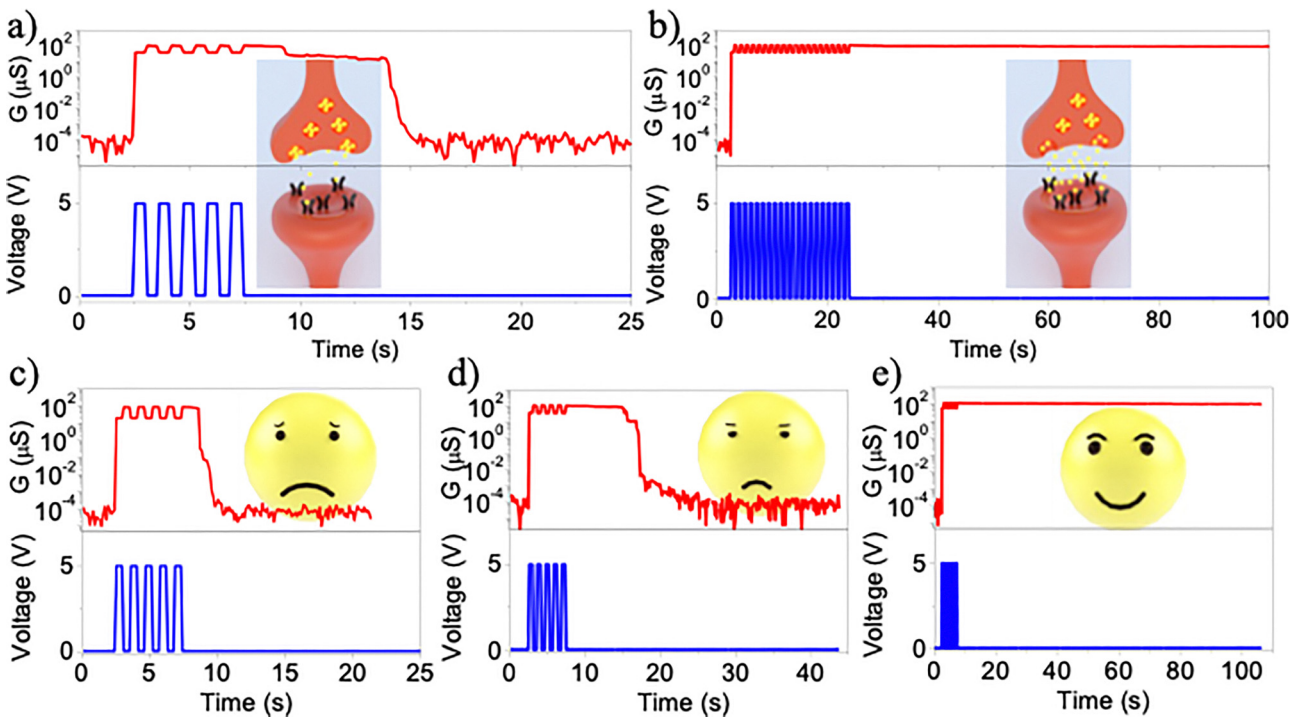

Fig. 4 Emulation of neuromorphic behaviors. Short-term plasticity (STP) and long-term plasticity (LTP) are demonstrated in the neuromorphic device using 5 V pulses with a 500 ms width and interval, and a 50 mV reading voltage. (a) and (b) A rehearsal-based STP to LTP transition is observed as the pulse number increases from 5 to 20 at a compliance current of 200 μA. (c)–(e) STP to LTP transition is also achieved by increasing the compliance current from 100 to 200 and 300 μA.

Open Access Article. Published on 21 April 2026. Downloaded on 5/12/2026 5:03:44 AM.
This article is licensed under a Creative Commons Attribution 3.0 Unported Licence.

the Atkinson–Shiffrin model, limited rehearsal of information facilitates short-term storage, whereas repeated rehearsal leads to long-term memory formation. To emulate this behavior, voltage pulses were applied with the configuration shown in Fig. S10 (SI). A 5 V pulse (500 ms width, 500 ms interval) was applied at a current compliance of 200 μA (Fig. 4a). Post pulsing, the conductance state was monitored with a small reading voltage of 50 mV. The number of pulses represented rehearsal events. For low rehearsal, such as 5 pulses, the conductance retention was found to be ~6 s, indicating short-term plasticity. Meanwhile, 20 pulses resulted in memory retention for more than 60 s, indicating long-term plasticity (Fig. 4b). This was also emulated using current compliance (I_{CC}) with the application of 5 pulses of 5 V (Fig. 4c–e). In general, lower current compliance leads to short-term plasticity, while higher current compliance leads to long-term potentiation. For 100 μA I_{CC}, the retention was 2–3 s, while increasing the I_{CC} resulted in increasing retention, and finally, for 300 μA, the device showed LTP with retention for more than 60 s, again highlighting the role of the input strength in transitioning from STP to LTP. Interestingly, the devices showed long-term stability, retaining switching characteristics and synaptic features for over 6 months (Fig. S11, SI). The transition from short-term plasticity (STP) to long-term potentiation (LTP) is governed by the pulse number and current compliance. Lower pulse numbers or compliance result in weak, unstable filaments that decay rapidly (STP), whereas higher values form thicker and more stable conductive pathways, leading to prolonged retention (LTP).[54]

Another critical cognitive phenomenon observed in daily life is arousal-dependent learning and memory, classically described by the Yerkes–Dodson law.[52] In their study, Yerkes and Dodson demonstrated that mice solved a maze most effectively under moderate electrical shock (*i.e.* moderate arousal), whereas both lower and higher shock intensities impaired task performance. This established the principle that learning efficiency follows an inverted-U dependence on arousal,[55]

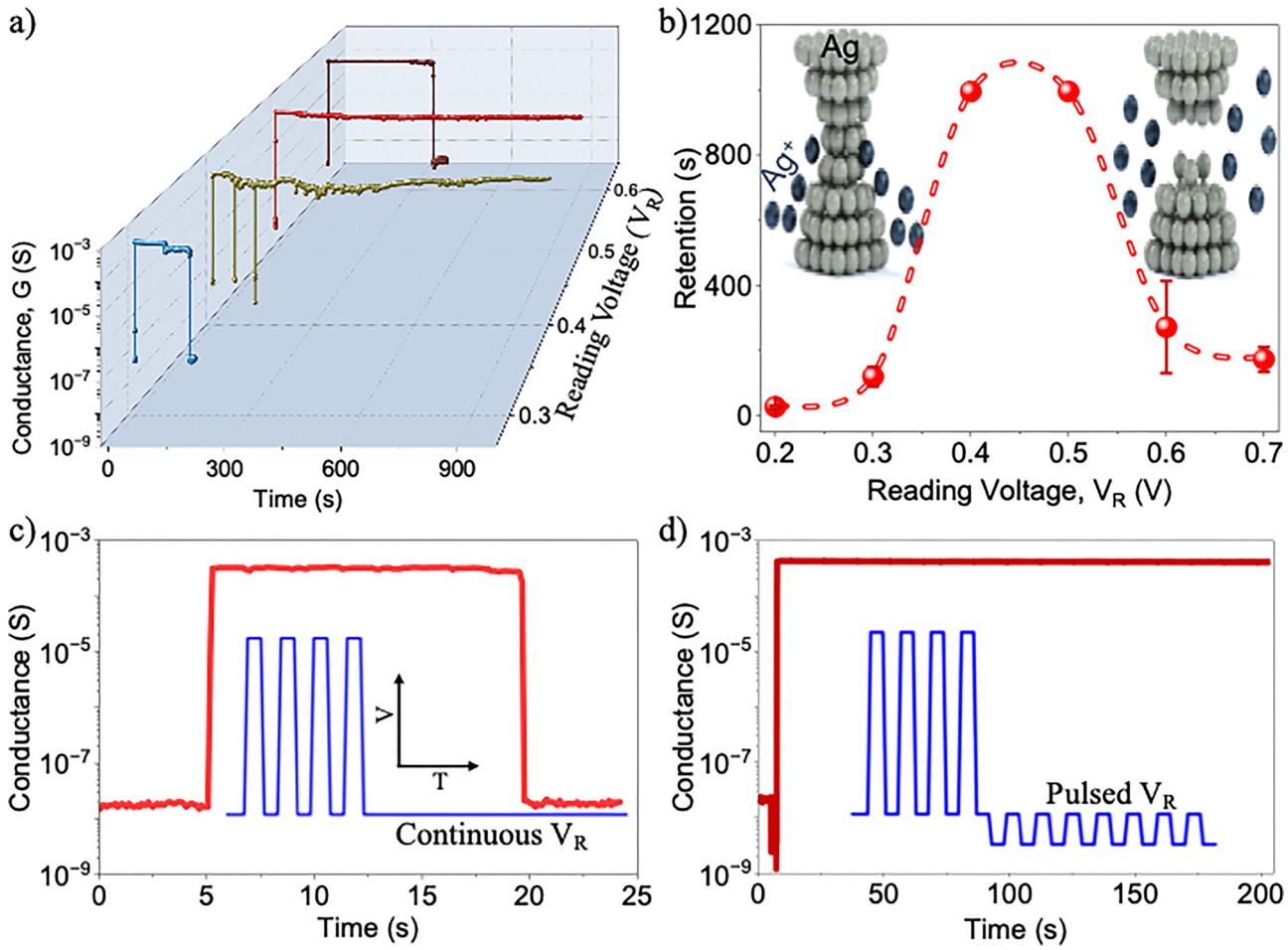

Fig. 5 Brain-inspired arousal-dependent learning in an Ag-based neuromorphic device. (a) Memory retention measured at different reading voltages (V_R), where the reading voltage serves as an analog of arousal strength. Low arousal (≤0.3 V) and high arousal (≥0.6 V) yield poor retention, whereas moderate arousal levels (0.4–0.5 V) produce significantly enhanced retention. (b) Inverted-U dependence of retention on reading voltage, mimicking the Yerkes–Dodson law. The inset illustrates the proposed mechanism: weak filament stability due to insufficient electric fields (left) and Joule-heating-induced filament dissolution at high electric fields (right). (c) Retention behavior under a continuous 0.8 V reading voltage applied during a 5 V pulsing sequence (inset), resulting in short retention due to strong Joule heating. (d) Applying the same reading voltage in a pulsed manner (inset) significantly extends the retention, confirming that reduced Joule heating enhances filament stability.

 This journal is © The Royal Society of Chemistry 2026

Open Access Article. Published on 21 April 2026. Downloaded on 5/12/2026 5:03:44 AM. This article is licensed under a Creative Commons Attribution 3.0 Unported Licence.

widely recognized in psychology as the basis for performance breakdown or "choking under pressure".[56] At the neurophysiological level, such behavior is frequently attributed to dopamine-mediated modulation of synaptic plasticity, where moderate dopamine release enhances learning, whereas excessive release becomes detrimental.[55]

Emulating this form of arousal-dependent cognitive behavior in neuromorphic hardware is an important step toward developing more adaptive and biologically faithful artificial intelligence systems.[57] However, demonstrations of Yerkes–Dodson-type responses in solid-state neuromorphic devices remain scarce. In this work, we assign the reading voltage in our Ag-based neuromorphic device as an analog of neurophysiological arousal intensity, with low, moderate, and high voltages corresponding to low, optimal, and over-arousal states, respectively. The read voltage is treated as an analog of the arousal strength, as it directly influences the retention characteristics of the device. As shown in Fig. 5a, reading voltages below 0.3 V resulted in low retention (<150 s), analogous to under-arousal. In contrast, a moderate reading voltage in the range of 0.4–0.5 V produced a substantial increase in retention (>900 s), indicating an optimal-arousal regime that maximizes performance. Increasing the reading voltage beyond 0.6 V again reduced the retention (~ 200 s) due to overstimulation. This inverted-U dependence (Fig. 5b) closely mirrors the classical Yerkes–Dodson arousal-performance relationship, with 0.4–0.5 V representing the optimal operational window for learning-like behavior in this device. These results highlight the capability of the device to emulate higher-order cognitive functions, enabling more advanced neuromorphic artificial intelligence architectures.

Because real biological inverted-U responses are often asymmetric, we modeled the retention–voltage relationship using an asymmetric (split-σ) Gaussian function (Fig. S12 and eqn (S1), SI), where the left and right widths (σ_L, σ_R) capture the differential sensitivity of the device to low-voltage (under-arousal) and high-voltage (over-arousal) conditions. The fitting reveals that the retention is more sensitive to the low-voltage side ($\sigma_L = 0.064 < \sigma_R = 0.1$, Note S1, SI), suggesting that insufficient electric-field stabilization leads to the rapid dissolution of Ag filaments. We attribute the decline in retention at high reading voltages to Joule-heating-assisted oxidation followed by dissolution of the conductive filament, resulting in filament instability and degraded performance. To support this mechanism, we compared the retention behavior under continuous and pulsed reading voltages. A pulsed reading voltage reduces the average thermal load, thereby suppressing Joule heating and improving filament stability. As shown in Fig. 5c, a continuous reading voltage of 0.8 V applied during and after the pulsing sequence yielded a retention of only ~ 7 s. However, when the reading voltage was applied in a pulsed manner (Fig. 5d), the retention significantly increased to >200 s. This clear enhancement confirms that reducing Joule heating mitigates filament oxidation and dissolution, validating the proposed physical mechanism underlying the inverted-U learning behavior.

Conclusions

In summary, this study presents a simple yet effective optical printing–annealing strategy for fabricating self-formed Ag nanostructures that act as active elements in neuromorphic devices. By tuning the printing and annealing conditions, the resulting Ag synaptic network morphologies were optimized to emulate essential synaptic functionalities. The devices exhibit stable resistive switching and reliably reproduce key forms of biological plasticity, including short- and long-term potentiation. Notably, we also demonstrate arousal-dependent performance behavior, classically described by the Yerkes–Dodson law, by mapping the reading voltage as the arousal strength. The retention was high at an optimal read voltage, while both lower and higher voltages impaired performance, resulting in a characteristic inverted-U trend. This behavior was adequately described using an asymmetric Gaussian model, and further study revealed that the observed decline at high voltages is attributed to Joule-heating-induced filament destabilization. Thus, by leveraging self-organized architectures with intrinsic disorder and emergent electrical behavior, this approach provides a promising route toward hardware that more closely reflects the adaptive, nonlinear nature of biological neural systems. Overall, this work highlights the feasibility of optically processed Ag nanostructures for neuromorphic applications and underscores their robustness and adaptability, paving the way for future low-power, flexible, and biologically inspired computing platforms.

Experimental section

Materials

$AgNO_3$ ($\geq 99.0\%$, Merck Life Science Private Limited), trisodium citrate dihydrate ($\geq 99\%$, Merck Life Science Private Limited).

Optical printing and annealing

Particulate silver films were deposited using a white-light-assisted optical printing method. Light from a DLP projector was coupled to a Nikon microscope *via* an eyepiece and a Keplerian lens arrangement (−100 mm and 300 mm focal lengths) and directed through a dichroic mirror that primarily reflected the green component. Printing was performed with a 10× objective lens, enabling large-area deposition. Printed films were annealed on an IKA hotplate at 200 °C and 300 °C for various durations to obtain dewetted structures.

Device fabrication

Gold electrodes were defined by shadow masking, followed by thermal evaporation of a 50-nm Au layer under a vacuum of 7×10^{-6} Torr. Optical printing was carried out between the electrodes, and the films were annealed to form dewetted Ag structures to realize neuromorphic devices.

Device characterization

I–V and pulsed electrical measurements were performed with a Keysight B2901B source measure unit (retention time

Open Access Article. Published on 21 April 2026. Downloaded on 5/12/2026 5:03:44 AM.
This article is licensed under a Creative Commons Attribution 3.0 Unported Licence.

measurements were limited in some cases due to available sampling points). FESEM images were acquired using a Zeiss microscope and optical images with a Leica microscope, and UV–vis spectra with a JASCO V650 spectrometer. Nanoparticle size distributions were measured using a Horiba Scientific SZ-100 analyzer, and image analysis was conducted with FIJI (ImageJ).

Synthesis of silver nanoparticles

Silver nanoparticles were synthesized by the Lee–Meisel method.[53] Briefly, 17 mg of $AgNO_3$ was dissolved in 50 mL of deionized water and heated to 90 °C. A 40 mM trisodium citrate solution was added dropwise under magnetic stirring until the solution turned golden yellow.

Conflicts of interest

There are no conflicts to declare.

Data availability

The authors confirm that the data supporting the findings of this study are available within the article and its supplementary information (SI). Supplementary information: schematic representation of the projected image; UV-Vis spectroscopy and particle size analysis of the Ag nanoparticles; optical images of the dewetted patterns; fill factor analysis; FESEM images of the dewetted patte. See DOI: https://doi.org/10.1039/d6tc00516k.

Raw data that support the findings of this study are available from the corresponding author upon reasonable request.

Acknowledgements

The authors gratefully acknowledge the Manipal Academy of Higher Education for the facility and fund support.

Notes and references

1 J. Zhu, T. Zhang, Y. Yang and R. Huang, *Appl. Phys. Rev.*, 2020, **7**, 011312.
2 A. Mehonic, D. Ielmini, K. Roy, O. Mutlu, S. Kvatinsky, T. Serrano-Gotarredona, B. Linares-Barranco, S. Spiga, S. Savel'ev, A. G. Balanov, N. Chawla, G. Desoli, G. Malavena, C. Monzio Compagnoni, Z. Wang, J. J. Yang, S. G. Sarwat, A. Sebastian, T. Mikolajick, S. Slesazeck, B. Noheda, B. Dieny, T.-H. (Alex) Hou, A. Varri, F. Brückerhoff-Plückelmann, W. Pernice, X. Zhang, S. Pazos, M. Lanza, S. Wiefels, R. Dittmann, W. H. Ng, M. Buckwell, H. R. J. Cox, D. J. Mannion, A. J. Kenyon, Y. Lu, Y. Yang, D. Querlioz, L. Hutin, E. Vianello, S. S. Chowdhury, P. Mannocci, Y. Cai, Z. Sun, G. Pedretti, J. P. Strachan, D. Strukov, M. Le Gallo, S. Ambrogio, I. Valov and R. Waser, *APL Mater.*, 2024, **12**, 109201.
3 Y. Zhu, H. Mao, Y. Zhu, X. Wang, C. Fu, S. Ke, C. Wan and Q. Wan, *Int. J. Extreme Manuf.*, 2023, **5**, 042010.
4 S. Gao, X. Yi, J. Shang, G. Liu and R.-W. Li, *Chem. Soc. Rev.*, 2019, **48**, 1531–1565.
5 H. Seok, D. Lee, S. Son, H. Choi, G. Kim and T. Kim, *Adv. Electron. Mater.*, 2024, **10**, 2300839.
6 Y. Beilliard and F. Alibart, *Front. Nanotechnol.*, 2021, **3**, 779070.
7 S. Song, J. Kim, S. M. Kwon, J. Jo, S. K. Park and Y. Kim, *Adv. Intell. Syst.*, 2021, **3**, 2000119.
8 X. Ji, Z. Dong, G. Zhou, C. S. Lai, Y. Yan and D. Qi, *Electronics*, 2021, **10**, 3176.
9 Y. H. Jang, J. Han and C. S. Hwang, *InfoScience*, 2024, **1**, e12013.
10 M. Zhao, B. Gao, J. Tang, H. Qian and H. Wu, *Appl. Phys. Rev.*, 2020, **7**, 011301.
11 G. Zhou, Z. Wang, B. Sun, F. Zhou, L. Sun, H. Zhao, X. Hu, X. Peng, J. Yan, H. Wang, W. Wang, J. Li, B. Yan, D. Kuang, Y. Wang, L. Wang and S. Duan, *Adv. Electron. Mater.*, 2022, **8**, 2101127.
12 Y. Yu, M. Xiao, D. Fieser, W. Zhou and A. Hu, *J. Mater. Chem. C*, 2024, **12**, 3770–3810.
13 W. Chen, L. Song, S. Wang, Z. Zhang, G. Wang, G. Hu and S. Gao, *Adv. Electron. Mater.*, 2023, **9**, 2200833.
14 Z. Wang, M. Rao, R. Midya, S. Joshi, H. Jiang, P. Lin, W. Song, S. Asapu, Y. Zhuo, C. Li, H. Wu, Q. Xia and J. J. Yang, *Adv. Funct. Mater.*, 2018, **28**, 1704862.
15 G. Milano, F. Raffone, M. Luebben, L. Boarino, G. Cicero, I. Valov and C. Ricciardi, *ACS Appl. Mater. Interfaces*, 2020, **12**, 48773–48780.
16 J. D. Greenlee, W. L. Calley, M. W. Moseley and W. A. Doolittle, *IEEE Trans. Electron Devices*, 2013, **60**, 427–432.
17 H. Kang, J. Seo, H. Kim, H. W. Kim, E. R. Hong, N. Kim, D. Lee and J. Woo, *Micromachines*, 2022, **13**, 453.
18 S. Ambrogio, N. Ciocchini, M. Laudato, V. Milo, A. Pirovano, P. Fantini and D. Ielmini, *Front. Neurosci.*, 2016, **10**, 56.
19 S. La Barbera, D. R. B. Ly, G. Navarro, N. Castellani, O. Cueto, G. Bourgeois, B. De Salvo, E. Nowak, D. Querlioz and E. Vianello, *Adv. Electron. Mater.*, 2018, **4**, 1800223.
20 M. Xu, X. Mai, J. Lin, W. Zhang, Y. Li, Y. He, H. Tong, X. Hou, P. Zhou and X. Miao, *Adv. Funct. Mater.*, 2020, **30**, 2003419.
21 T. S. Rao, S. Kundu, B. Bannur, S. J. George and G. U. Kulkarni, *Nanoscale*, 2023, **15**, 7450–7459.
22 L. Zhao, Z. Fan, S. Cheng, L. Hong, Y. Li, G. Tian, D. Chen, Z. Hou, M. Qin, M. Zeng, X. Lu, G. Zhou, X. Gao and J. M. Liu, *Adv. Electron. Mater.*, 2020, **6**, 1900858.
23 S. Gao, G. Liu, H. Yang, C. Hu, Q. Chen, G. Gong, W. Xue, X. Yi, J. Shang and R. W. Li, *ACS Nano*, 2019, **13**, 2634.
24 C. Weber and I. Valov, in 2023 IEEE International Symposium on Circuits and Systems (ISCAS), IEEE, Monterey, CA, USA, 2023, pp. 1–4.
25 I. Valov, R. Waser, J. R. Jameson and M. N. Kozicki, *Nanotechnology*, 2011, **22**, 254003.
26 Z. Lv, H. Wang, J. Zheng, X. Zhao, G. Ding, Y. Wang, Y. Zhai, Q. Zhang, Y. Zhou, W. C. H. Choy and S. Han, *Adv. Mater.*, 2026, **38**, e18105.

 This journal is © The Royal Society of Chemistry 2026

Open Access Article. Published on 21 April 2026. Downloaded on 5/12/2026 5:03:44 AM. This article is licensed under a Creative Commons Attribution 3.0 Unported Licence.

27 Z. Lv, S. Zhu, Y. Wang, Y. Ren, M. Luo, H. Wang, G. Zhang, Y. Zhai, S. Zhao, Y. Zhou, M. Jiang, Y. Leng and S. Han, *Adv. Mater.*, 2024, **36**, 2405145.
28 T. S. Rao, S. J. George and G. U. Kulkarni, *Nanoscale Horiz.*, 2025, **10**, 1192–1202.
29 M. Pal, N. S. Vidhyadhiraja and G. U. Kulkarni, *Adv. Funct. Mater.*, 2025, **35**, 2425635.
30 S. Dai, X. Wu, D. Liu, Y. Chu, K. Wang, B. Yang and J. Huang, *ACS Appl. Mater. Interfaces*, 2018, **10**, 21472–21480.
31 A. H. Jaafar, R. J. Gray, E. Verrelli, M. O'Neill, S. M. Kelly and N. T. Kemp, *Nanoscale*, 2017, **9**, 17091–17098.
32 B. Sueoka and F. Zhao, *J. Phys. Appl. Phys.*, 2022, **55**, 225105.
33 R. A. John, F. Liu, N. A. Chien, M. R. Kulkarni, C. Zhu, Q. Fu, A. Basu, Z. Liu and N. Mathews, *Adv. Mater.*, 2018, **30**, 1800220.
34 D. Sarkar, J. Tao, W. Wang, Q. Lin, M. Yeung, C. Ren and R. Kapadia, *ACS Nano*, 2018, **12**, 1656–1663.
35 Z. Kuncic, T. Nakayama and J. Gimzewski, *Neuromorphic Comput. Eng.*, 2022, **2**, 040201.
36 A. Diaz-Alvarez, R. Higuchi, P. Sanz-Leon, I. Marcus, Y. Shingaya, A. Z. Stieg, J. K. Gimzewski, Z. Kuncic and T. Nakayama, *Sci. Rep.*, 2019, **9**, 14920.
37 Q. Li, A. Diaz-Alvarez, D. Tang, R. Higuchi, Y. Shingaya and T. Nakayama, *ACS Appl. Mater. Interfaces*, 2020, **12**, 50573–50580.
38 G. Milano, G. Pedretti, M. Fretto, L. Boarino, F. Benfenati, D. Ielmini, I. Valov and C. Ricciardi, *Adv. Intell. Syst.*, 2020, **2**, 2000096.
39 M. D. Pike, S. K. Bose, J. B. Mallinson, S. K. Acharya, S. Shirai, E. Galli, S. J. Weddell, P. J. Bones, M. D. Arnold and S. A. Brown, *Nano Lett.*, 2020, **20**, 3935–3942.
40 A. Sattar, S. Fostner and S. A. Brown, *Phys. Rev. Lett.*, 2013, **111**, 136808.
41 J. B. Mallinson, Z. E. Heywood, R. K. Daniels, M. D. Arnold, P. J. Bones and S. A. Brown, *Nanoscale*, 2023, **15**, 9663–9674.
42 B. Bannur and G. U. Kulkarni, *Mater. Horiz.*, 2020, **7**, 2970–2977.
43 B. Bannur, B. Yadav and G. U. Kulkarni, *ACS Appl. Electron. Mater.*, 2022, **4**, 1552–1557.
44 T. S. Rao, I. Mondal, B. Bannur and G. U. Kulkarni, *Discov. Nano*, 2023, **18**, 124.
45 M. Franco, A. Kiazadeh, R. Martins, S. Lanceros-Méndez and E. Carlos, *Adv. Electron. Mater.*, 2024, **10**, 2400212.
46 K. Monisha, K. Suresh, A. Bankapur and S. D. George, *Anal. Chim. Acta*, 2024, **1317**, 342903.
47 M. Herber, D. Lengle, S. R. Valandro, M. Wehrmeister and E. H. Hill, *Nano Lett.*, 2023, **23**, 6308–6314.
48 K. Monisha, K. Suresh, A. Bankapur and S. D. George, *Sens. Actuators, B*, 2023, **377**, 133047.
49 M. D. Ganeriwala, R. Motos Espada, E. G. Marin, J. Cuesta-Lopez, M. Garcia-Palomo, N. Rodríguez, F. G. Ruiz and A. Godoy, *ACS Appl. Mater. Interfaces*, 2024, **16**, 49724–49732.
50 L. Yang, H. Hu, A. Scholz, F. Feist, G. Cadilha Marques, S. Kraus, N. M. Bojanowski, E. Blasco, C. Barner-Kowollik, J. Aghassi-Hagmann and M. Wegener, *Nat. Commun.*, 2023, **14**, 1103.
51 B. Bannur, M. Kolikkaje, S. Mysuru Shivalingegowda and S. Daniel George, *Mater. Horiz.*, 2025, **12**, 4875–4883.
52 R. M. Yerkes and J. D. Dodson, *J. Comp. Neurol. Psychol.*, 1908, **18**, 459–482.
53 P. C. Lee and D. Meisel, *J. Phys. Chem.*, 1982, **86**, 3391–3395.
54 S. La Barbera, D. Vuillaume and F. Alibart, *ACS Nano*, 2015, **9**, 941–949.
55 R. Cools and M. D'Esposito, *Biol. Psychiatry*, 2011, **69**, e113–e125.
56 Z. Liu and R. Tang, *Curr. Psychol.*, 2024, **43**, 36700–36713.
57 X. Zhang, J.-X. Pang, Y.-H. Kang, Y.-F. Wang, W.-W. Zhao and J.-J. Xu, *Anal. Chem.*, 2025, **97**, 22548–22554.